Journal of Physics Communications

PAPER • OPEN ACCESS

# Probing tip-induced attractive deformation of graphite surfaces through wave function dissipation in field emission resonance

To cite this article: Shitha Valsan Korachamkandy *et al* 2022 *J. Phys. Commun.* **6** 075010

IOP Publishing J. Phys. Commun. 6 (2022) 075010 https://doi.org/10.1088/2399-6528/ac819d

Journal of Physics Communications

CrossMark

OPEN ACCESS

RECEIVED
28 March 2022

REVISED
12 July 2022

ACCEPTED FOR PUBLICATION
15 July 2022

PUBLISHED
25 July 2022



PAPER

# Probing tip-induced attractive deformation of graphite surfaces through wave function dissipation in field emission resonance

**Shitha Valsan Korachamkandy[1,2,3], Shin-Ming Lu[3], Wei-Bin Su[3], Wen-Yuan Chan[3], Ho-Hsiang Chang[3], Horng-Tay Jeng[3,4], Chih-Hao Lee[1] and Chia-Seng Chang[3]**

[1] Department of Engineering and System Science, National Tsing Hua University, Hsinchu 30013, Taiwan
[2] Nano Science and Technology Program, Taiwan International Graduate Program, Academia Sinica, Nankang, Taipei 11529, Taiwan
[3] Institute of Physics, Academia Sinica, Nankang, Taipei 11529, Taiwan
[4] Department of Physics, National Tsing Hua University, Hsinchu 30013, Taiwan

**E-mail:** wbsu@phys.sinica.edu.tw

**Keywords:** graphite surface, field emission resonance, wave function dissipation, tip-induced attractive deformation

Supplementary material for this article is available online

## Abstract

We studied wave function dissipation (WFD) in field emission resonance (FER) by performing scanning tunneling microscopy on the highly oriented pyrolytic graphite (HOPG) and Ag(111) surfaces under two conditions: (1) the same current and FER number; (2) the same tip structure but different currents. Under the first condition, we observed that the decay rate corresponding to the WFD exhibited a larger variation on the HOPG surface than it did on the Ag(111) surface. Under the second condition, the decay rate was nearly independent of the FER electric field for the Ag(111) surface; by contrast, it was linearly proportional to the FER electric field for the HOPG surface. These remarkable differences can be attributed to the factors that the tip-induced attractive deformation caused by the electrostatic force was considerably more prominent on the HOPG surface than on the Ag(111) surface and that the deformed HOPG top layer had a unique electronic structure similar to that of single-layer graphene.

## 1. Introduction

An electric field of 0.1–0.3 V/Å in the junction of scanning tunneling microscope (STM) is inherently intrusive to the surface properties of materials. For example, this strong electric field can perturb electronic states such as the surface state, quantum well state, and transmission resonance, causing shifts in the state energy [1–3]. Moreover, this electric field can induce a local expansion deformation in Pb films through the STM tip [4], engendering a tip-induced attractive deformation (TIAD) caused by the corresponding electrostatic force. This TIAD is greater for the suspended graphene [5, 6]. Therefore, a TIAD can be expected on the graphite surface beneath an STM tip because of the weak van der Waals force between atomic layers of graphite. Nevertheless, this has never been detected, possibly because no tool is available for TIAD monitoring. A previous study observed giant corrugation of carbon atoms on a graphite surface by using an STM, which is due to the deformation induced by repulsive interatomic forces [7]. Moreover, through the deformation due to the contact between the atomic force microscopy tip and graphene, atomic-scale frictional characteristics of graphene can be resolved [8, 9].

Field emission resonance (FER) [10] is a quantum phenomenon occurring in an STM junction when a negative and high bias voltage is applied to the STM tip [11, 12]. Although FER originates from electrons tunneling into quantized states in a vacuum, its features such as energy, intensity, linewidth, and number, can provide information about the properties of the surface and STM tip. Consequently, FER has been a versatile technique to explore various phenomena [13–39]. For example, the FER number can reflect the sharpness of an STM tip; a higher FER number indicates a sharper tip [17, 35, 36]. In addition, previous studies demonstrated that the FER observed on the reconstructed surfaces revealed spatial variation in linewidth [32–34]. This linewidth variation can be attributed to the local change of electron transmissivity [34]. These studies have motivated us to investigate whether electron transmissivity varies according to the TIAD on the graphite, and therefore, the linewidth is sensitive to the TIAD. For this exploration, a material whose surface does not deform easily was required. Ag(111) was selected because the metallic bond is considerably stronger than a van der Waals force. Our exploration results revealed that at the same FER number, the linewidth of first-order FER exhibited a significantly larger variation on the graphite surface than it did on the Ag(111) surface, indicating that FER can be used to monitor the TIAD of graphite. To further verify this finding, we observed the variation in linewidth with increasing current for the graphite and Ag(111) surfaces. Furthermore, our density functional theory (DFT) calculations demonstrated that the TIAD of the graphite surface could transform the electronic properties of the graphite top layer to be similar to those of the graphene, leading to variations in electron transmissivity with the TIAD level.

## 2. Experiment and calculation details

A clean graphite surface was prepared by cleaving the highly oriented pyrolytic graphite (HOPG) in air by using adhesive tape. A clean Ag(111) surface was prepared using ion sputtering followed by annealing at 600 °C for several cycles. An ultra-high-vacuum STM operated at 78 K or 5 K was used to observe FER on HOPG and Ag(111) surfaces. The FER detection was performed in Z–V (distance-voltage) spectroscopy by using Pt-Ir tips. For a Z–V measurement, the variation of the distance between the tip and surface was recorded with an active feedback, while the bias voltage was ramped from 3 to 10 V. The acquired Z–V spectra were differentiated using a numerical method to reveal the FER peaks.

The electronic structures were calculated using the projector augmented wave approach, as implemented in the Vienna *Ab initio* Simulation Package based on DFT. The Perdew—Burke—Ernzerhof form of the generalized gradient approximation was used for the exchange—correlation functional. The energy convergence threshold was set as $10^{-4}$ eV in self-consistent field calculations, and the energy convergence threshold was set as $10^{-3}$ eV for the structure optimizations. The lattice constant for Ag was determined to be 4.16 Å by minimizing the energy of the cell volume. Regarding the calculations performed for Ag, a $12 \times 12 \times 12$ k-point sampling grid was used to achieve energy convergence to within 1 meV/atom. To achieve high accuracy, we used a $24 \times 24 \times 24$ k-point grid to calculate the density of states (DOS) along the band symmetry points of Γ and L. Because the lattice constant for HOPG could not be obtained by minimizing the energy of cell volume, we set the experimental lattice constant $a_0$ to 2.46 Å for both HOPG and graphene and set $c_0$ to 6.78 Å for HOPG, in accordance with a previous study [40]. Regarding the calculations performed for HOPG, an $8 \times 8 \times 8$ k-point sampling grid was used to achieve energy convergence to within 1 meV/atom, and a $15 \times 15 \times 15$ k-point grid was used to achieve high accuracy in the DOS calculations. For the graphene calculations, an $11 \times 11 \times 1$ k-point sampling grid was used to achieve convergence. Moreover, a $15 \times 15 \times 1$ k-point grid with a vacuum thickness of 40 Å was used to achieve high accuracy in the DOS calculations.

## 3. Results and discussion

In the experiment, FER spectra were first acquired by repeatedly performing Z–V spectroscopy at 78 K and 30 pA on the HOPG and Ag(111) surfaces. Because a high voltage of up to 10 V was applied, the sharpness of the tip may change, causing variations in FER number. Moreover, the repeated execution of Z–V spectroscopy could lead to the destruction of the tip apex, resulting in the disappearance of FER peaks. When this situation occurred, voltage pulses were applied to sharpen the tip or replacing it with a new one. Thus, spectra with different FER numbers were obtained.

Because the work function of Ag(111) (4.74 eV) is close to that of HOPG (4.7 eV) [41], the same FER number indicates that the sharpness levels of STM tips on HOPG and Ag(111) were close. Therefore, we collected spectra of the same FER number on HOPG and Ag(111) surfaces. Figure 1 displays differential Z–V spectra with eight and nine FER peaks for HOPG [figures 1(a) and (b), respectively] and Ag(111) [figures 1(c) and (d), respectively]. The numbers indicated above peaks denote the FER orders. We focused on the linewidth ΔE of first-order FER (named FER 1 hereafter), which was extracted through Lorentzian fitting, as an example of FER 1 on the HOPG shown in figure 1(e). The dashed peaks in figures 1(a)–(d) are Lorentzian fittings, showing a high level consistency with all the FER 1 peaks. In our analysis, as illustrated in figure 2, the extracted linewidth values of FER 1 in spectra with the same FER number were sorted in ascending order and then separated into 10 groups. In each group, the spectrum with the highest ΔE value for FER 1 was selected to be displayed in figures 1(a)–(d). The numbers on the right-hand sides of the spectra were assigned according to the highest ΔE values in 10 groups. A larger number N in figures 1(a)–(d) corresponds to a higher ΔE value.

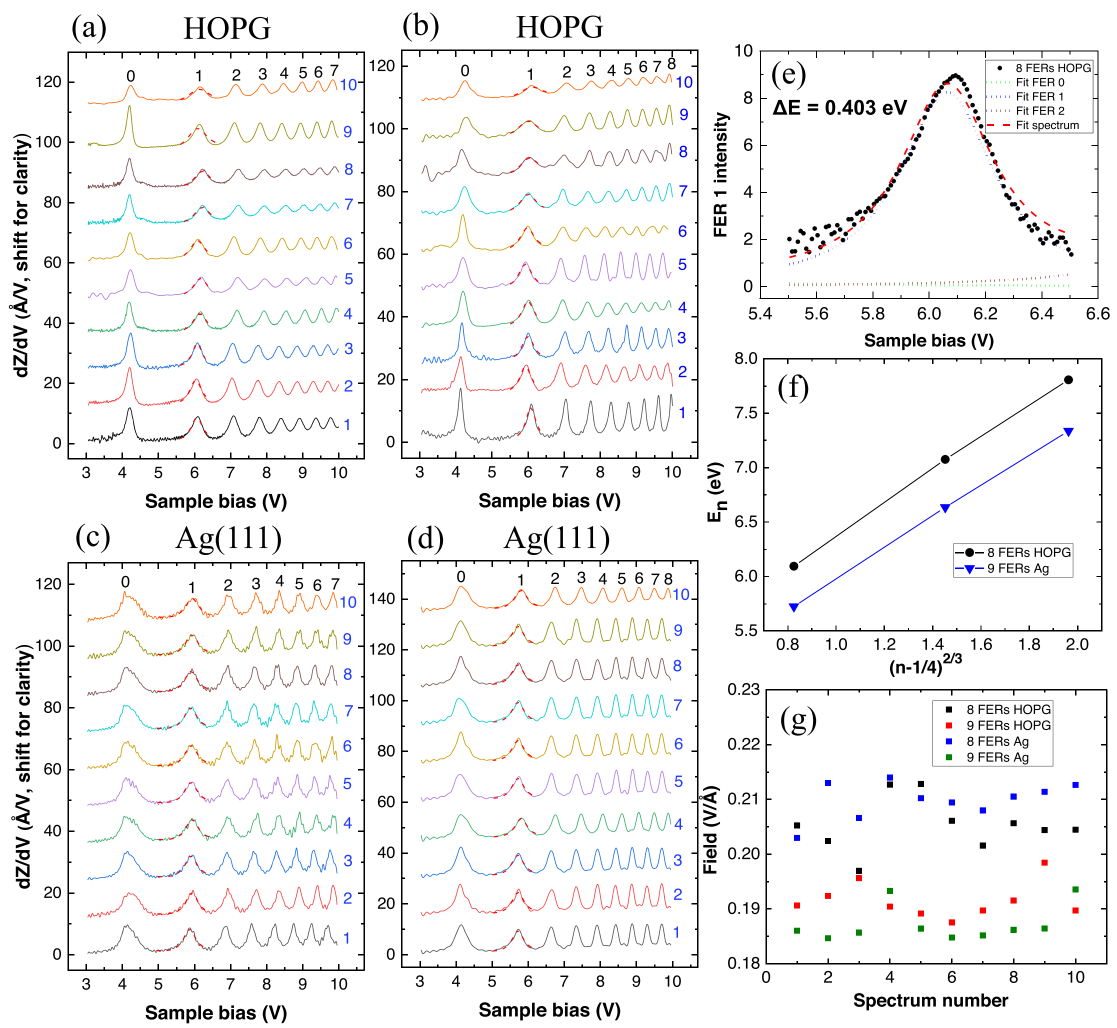


**Figure 1.** Differential Z–V spectra with eight and nine FER peaks for (a) and (b) HOPG surface and (c) and (d) Ag(111) surface. The numbers atop the FER peaks denote the FER orders. The dashed peaks represent the Lorentzian fitting results, revealing a good agreement with all FER 1 peaks. The spectrum numbers at the right-hand side were assigned according to the values of the FER 1 linewidth. (e) Example of the $\Delta E$ value for FER 1 extracted through Lorentzian fitting for the HOPG surface. (f) Plot of $E_n$ versus $(n-1/4)^{2/3}$ for n = 1, 2, 3 for the eight FER peaks for the HOPG surface and nine peaks for the Ag(111) surface, demonstrating a linear relation. Through the slope in the plot, $F_{FER}$ could be derived. (g) $F_{FER}$ for FER 1 in each spectrum in (a)–(d), indicating two groups established in terms of FER number for both the HOPG or Ag(111) surfaces.

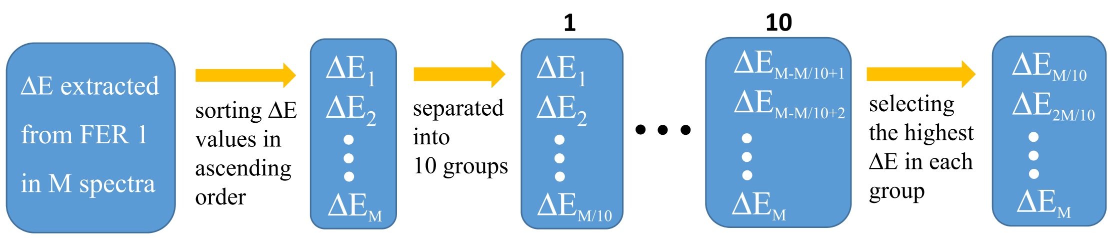


**Figure 2.** Steps for selecting spectra to display in figures 1(a)–(d).

Although the overall potential in the STM junction along the surface normal is not linear [36], a previous study demonstrated that the linear potential is a good approximation for the formation of FER quantized states of order n = 1, 2, 3 so that the electric field $F_{FER}$ is constant for these three states [38]. The corresponding FER energies $E_n$ can be expressed with the energies of quantized states in the triangular potential well [42] as follows:

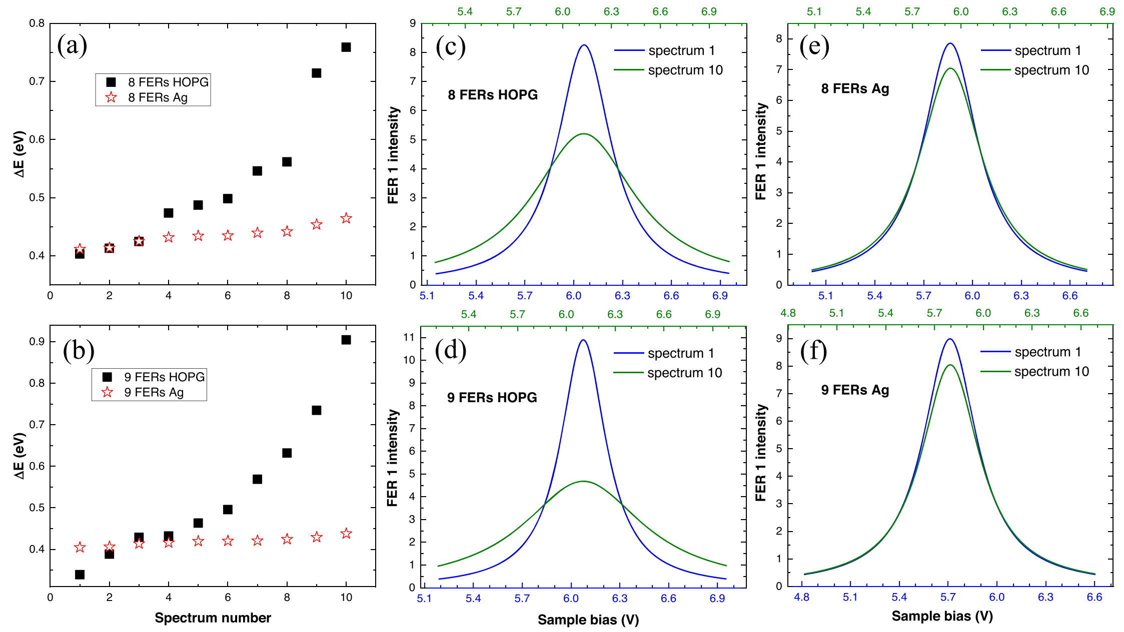


**Figure 3.** (a) Linewidth of FER 1 for the HOPG and Ag(111) surfaces versus spectrum number N for eight FER peaks and (b) nine FER peaks. (c) and (d) Line shapes of FER 1 for spectra 1 and 10 for the HOPG surface, respectively, and (e) and (f) those for the Ag(111) surface, respectively.

$$\mathrm{E_n} = \mathrm{E_{vac}} + \alpha F_{FER}{}^{\frac{2}{3}}\left(n - \frac{1}{4}\right)^{\frac{2}{3}}, \tag{1}$$

where $\mathrm{E_{vac}}$ is the vacuum level and

$$\alpha = \left(\frac{\hbar^2}{2m}\right)^{\frac{1}{3}}\left(\frac{3\pi \mathrm{e}}{2}\right)^{\frac{2}{3}}. \tag{2}$$

Thus, the plot of $\mathrm{E_n}$ versus $(\mathrm{n}-1/4)^{2/3}$ is linear for n = 1, 2, 3, as displayed in figure 1(f) for 8 FER peaks on HOPG and 9 FER peaks on Ag(111). $\mathrm{F_{FER}}$ can be obtained from calculating the slope in the plot divided by $\alpha$ to the power of 3/2. Figure 1(g) presents the $\mathrm{F_{FER}}$ values for FER 1 in the spectra displayed in figures 1(a)–(d); as indicated in this figure, two separate groups were observed in terms of FER number for both the HOPG and Ag(111) cases. On average, $\mathrm{F_{FER}}$ value for the eight FER peaks was higher than that for the nine peaks and at the same FER number, the $\mathrm{F_{FER}}$ value for the HOPG case was similar to that for the Ag(111) case. Figure 3(a) exhibits that for the spectra with eight FER peaks, the FER 1 linewidths on both HOPG and Ag(111) increased with spectrum number N; nevertheless, the $\Delta$E variation between spectra 10 and 1 for HOPG was considerably larger than that for Ag(111). This difference was also observed in the spectra with nine FER peaks [figure 3(b)]. Consequently, the line shapes of FER 1 in spectra 1 and 10 for HOPG were clearly different [figures 3(c) and (d)], but those for Ag(111) only had slight changes [figures 3(e) and 3(f)].

Previous studies revealed that FER electrons can leave the quantized state through light emission [16, 17] or surface transmission [34], which indicates that the wave function of FER electrons is not static but can be dissipated. In spite of wave function dissipation (WFD), before leaving FER state, the electron moves to and fro in round trips in the STM junction. Due to WFD, the probability P(i) that electrons remain in the quantized state may decay with the number i of round trips at a rate of D which is the sum of the electron transmissivity $\Gamma_t$ and the decay rate per round trip due to light emission $\Gamma_l$. P(i) can be defined as follows

$$\mathrm{P(i)} = (1 - \mathrm{D})^{\mathrm{i}}. \tag{3}$$

Equation (3) indicates that the probability that a resonant electron stays in FER state for (i − 1) round trips but exits FER state in the ith round trip is P(i − 1) − P(i). The average number of round trips ⟨i⟩ of all resonant electrons is as follows:

$$\langle \mathrm{i} \rangle = \sum_{\mathrm{i}=1}^{\mathrm{i}=\mathrm{i_{max}}} \mathrm{i}[\mathrm{P(i-1)} - \mathrm{P(i)}], \tag{4}$$

where $\mathrm{i_{max}}$ is the maximum number of round trips for which a resonant electron can stay in FER state, depending on the number of all resonant electrons. Using equations (3) and (4), ⟨i⟩ = 1/D is obtained (see supplementary

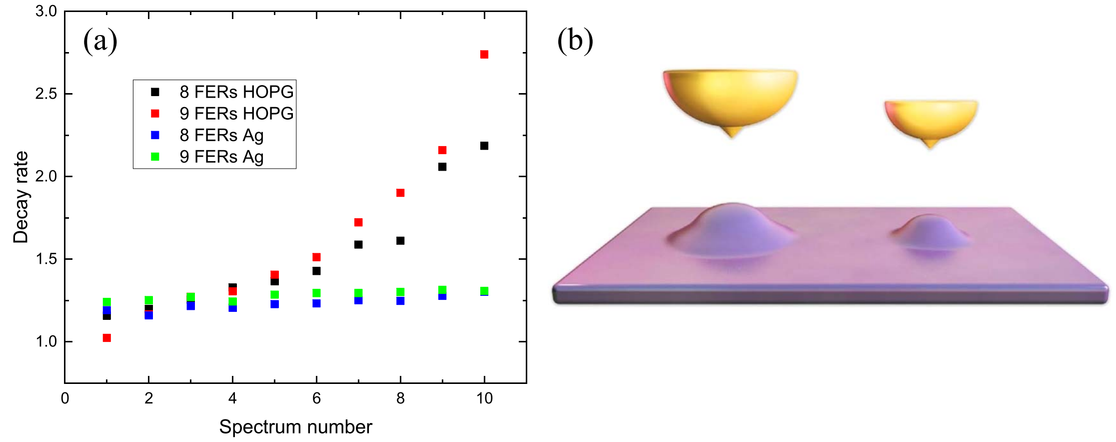


**Figure 4.** (a) Decay rate of FER 1 for the HOPG and Ag(111) surfaces versus the spectrum number for eight and nine FER peaks. (b) Schematic of two deformation levels induced by two STM tips with the same sharpness but different bases for the HOPG surface. The deformation is shown to be dome shaped, with a greater dome height and wider dome diameter indicating a larger deformation level.

material (available online at stacks.iop.org/JPCO/6/075010/mmedia)). Resonant electrons move back and forth within a distance $s = (E_n - E_{vac})/eF_{FER}$ between the surface and the classical turning point. As a result, the round-trip time $t$ for resonant electron can be calculated using $2s = eF_{FER}\, t^2/m$. By combining this equation with equations (1) and (2), $t = \beta \frac{\left(n - \frac{1}{4}\right)^{\frac{1}{3}}}{F_{FER}^{\frac{2}{3}}}$ is obtained, where $\beta = \left(\frac{3m\hbar\pi}{e^2}\right)^{\frac{1}{3}}$. The mean lifetime of resonant electrons in FER state, proportional to $1/\Delta E$, can be defined as $\langle i \rangle\, t$. Consequently, $\Delta E$ is proportional to D. This relation can explain that on reconstructed Au(111) surface, FER has a larger $\Delta E$ at the ridge area with a higher $\Gamma_t$ (D), leading to a spatial variation of FER peak intensity [34] (see supplementary material).

For $n = 1$, D can be represented by a quantity $(0.75)^{1/3}\Delta E/F_{FER}^{2/3}$. Thus, given $\Delta E$ and $F_{FER}$, we can calculate D for each FER 1 peak in figure 1. Figure 4(a) displays the variation of the D values for FER 1 for HOPG and Ag(111) versus N for the spectra with eight and nine FER peaks. Although the D value for Ag(111) ($D_{Ag}$) remained nearly unchanged as N varied, the D value for HOPG ($D_{HOPG}$) rapidly increased with N for $N > 5$. We suggest that this difference could be attributed to the TIAD caused by the electrostatic force in STM junction and D proportional to the TIAD level (discussed later). The TIAD was more prominent on the HOPG surface because the metallic bond in Ag crystals is considerably stronger than the van der Waals force between atomic layers in HOPG. Therefore, $D_{HOPG}$ value exhibited a larger variation. However, the sharpness levels of the STM tip were close because FER number was the same. The sharpness level was unable to explain why the $D_{Ag}$ value was nearly constant but the $D_{HOPG}$ value varied. It is well accepted that an STM tip is composed of a base with a radius of tens of nanometers and a protrusion whose open angle determines the tip sharpness. Therefore, STM tips may have the same sharpness but different base radii. According to a theoretical study [43], when the distance d between the tip and surface is smaller than the base radius R, the electrostatic force F between them is as follows:

$$F = \pi\varepsilon_0 V_0^2 R/d, \tag{5}$$

where $V_0$ is the applied bias voltage. Therefore, a tip with a larger base radius can engender a stronger electrostatic force, causing a larger deformation level on the HOPG surface, and vice versa [figure 4(b)]. The TIAD is similar to be dome shaped. A wider dome diameter and greater height are noted to be associated with a higher TIAD level. Because Ag crystals do not deform easily, $D_{Ag}$ is insensitive to the base radius. Using equation (5), the electrostatic force can be estimated by assuming $R = 30$ nm and $d = 2$ nm for FER 1 whose energy is 6 eV, which is approximately 15 nN.

The TIAD probed by the FER linewidth demonstrated above was performed at the same current under different tip bases. Actually the electrostatic force can be tuned by changing the current. Accordingly, we also observed FER 1 $\Delta E$ values for HOPG and Ag(111) at 5 K under different currents. Figure 5(a) displays the FER spectra for HOPG at 0.01–1 nA, and figure 5(b) shows those for Ag(111) at 0.03–10 nA. As exhibited in both figures, when the current increased, the energy of the FER 1 peak (denoted by 1) moved toward high energy [39], indicating that the $F_{FER}$ of FER 1 increased with the applied current. Figure 5(c) depicts smooth plots of $F_{FER}$ versus current, implies that the tip structures on both surfaces were unchanged as the current increased. Figure 5(d) exhibits that FER 1 $\Delta E$ values enlarged with the current for both cases. On the basis of the results illustrated in figures 5(c) and (d), we calculated $D_{HOPG}$ and $D_{Ag}$ as a function of $F_{FER,}$ and figure 6(a) presents a plot of the calculation results. Figure 6(a) reveals a considerable disparity that $D_{HOPG}$ was linearly proportional

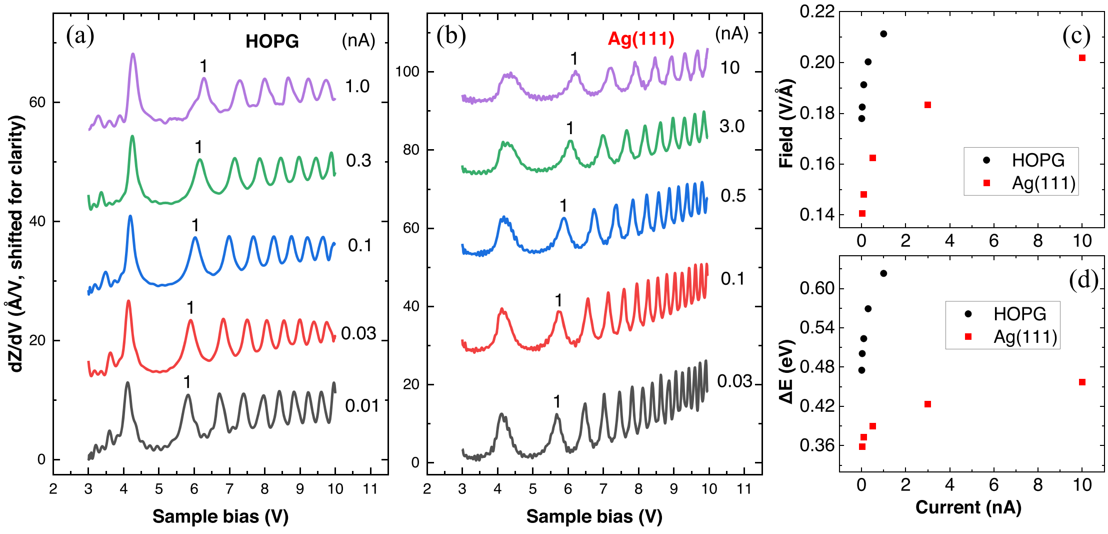


**Figure 5.** (a) FER spectra for the HOPG surface at 0.01–1 nA, and (b) those for the Ag(111) surface for 0.03–10 nA. (c) $F_{FER}$ plots as a function of current for the HOPG and Ag(111) surfaces. (d) FER 1 $\Delta E$ plots as a function of current for the HOPG and Ag(111) surfaces.

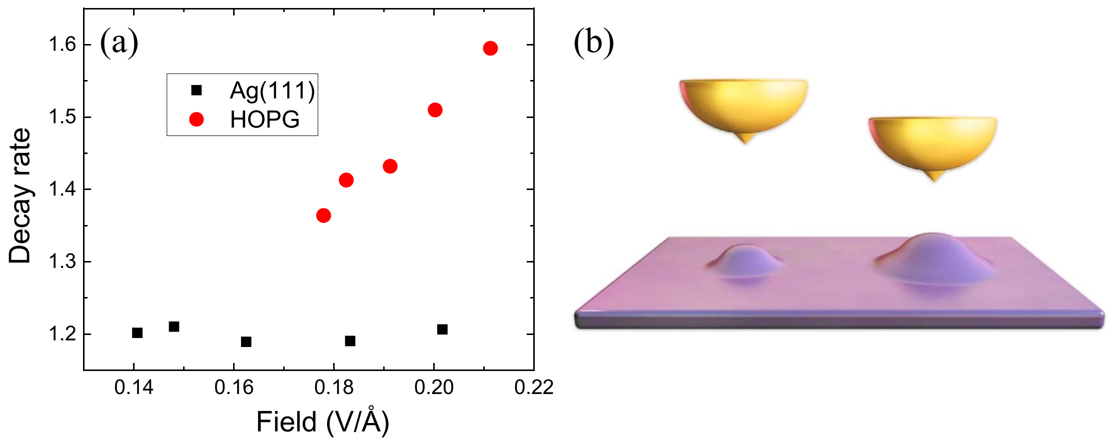


**Figure 6.** (a) Decay rate of FER 1 as a function of $F_{FER}$ for the HOPG and Ag(111) surfaces based on the data in figures 5(c) and (d). (b) Schematic of the HOPG surface deformation induced by an STM tip, which was larger when the distance between the tip and the surface was smaller.

to $F_{FER}$, whereas $D_{Ag}$ was nearly independent of $F_{FER}$. Because the electrostatic force enhances with increasing $F_{FER}$, figure 5(a) reflects that the TIAD on the HOPG surface was considerably larger than that on Ag(111), consistent with the results in figure 4(a). For increasing the current, the tip was controlled through the STM feedback, moving it closer to the surface. Accordingly, the electrostatic force was enhanced, attracting and displacing the HOPG surface upward. As a result, the TIAD level was higher (lower) at a shorter (longer) tip-surface distance, as visualized in figure 6(b).

Because HOPG and Ag(111) have no energy gap above their vacuum levels, the $\Gamma_l$ fluctuation caused by quantum trapping effect [38] is weak. Consequently, D was determined to be dependent only on $\Gamma_t$ in this study. A previous study suggested that $\Gamma_t$ is proportional to the DOS [34], signifying that the difference between $D_{HOPG}$ and $D_{Ag}$ can be explained by the DOS. Figure 7 depicts DOS values derived through DFT calculations for the HOPG, single-layer graphene, and Ag(111) surface. The DOS values derived at the FER 1 energy of approximately 6 eV were comparable for HOPG and Ag(111), explaining that $D_{HOPG}$ and $D_{Ag}$ values are close at $N < 5$ in figure 4(a). Therefore, the situation can occur on HOPG that the tip base is too small to induce the deformation.

As mentioned, the $D_{HOPG}$ value exhibited larger variations [figure 4(a)] and were linearly proportional to $F_{FER}$ [figure 6(a)], indicating that the DOS increases with the TIAD level. As displayed in figure 7, at approximately 6 eV, the DOS value of graphene was considerably greater than that of the HOPG surface. This notable DOS difference suggests that the electronic structure of the top HOPG layer gradually approaches that of

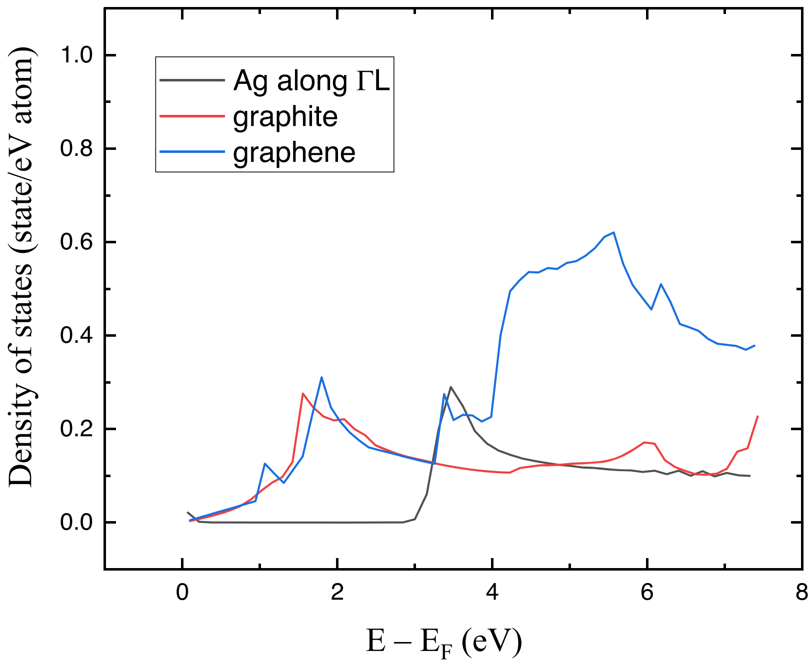


**Figure 7.** The DOS values for the HOPG, single-layer graphene, and the Ag(111) surface, derived using the DFT calculations.

the graphene as the TIAD level increased, thus increasing the corresponding DOS value. Moreover, because HOPG is a semimetal, it might not be able to behave like a metal to wholly block the penetration of the electric field in STM junction into deeper layers, but the top layer can effectively reduce the electric field. Consequently, the electrostatic force on deeper layers would be weaker than that on the top layer. The TIAD levels of deeper layers would be lower than that of top layer. The distances between the top layer and deeper layers are larger than those in HOPG without electrostatic force. Therefore, the electrostatic force in the STM junction locally attracts the top layer to be away from the second layer, which could effectively produce a quasi-graphene layer beneath the tip on the HOPG surface.

We measured the distance change ($\Delta Z$) in the Z–V spectrum corresponding to the differential spectrum of $N = 1$ in figures 1(a)–(d) for a bias voltage ranging from 3 to 10 V. The results show that distance changes are 30.0 and 34.1 Å for 8 and 9 FER peaks in the HOPG case, and 30.4 and 35.4 Å for 8 and 9 FER peaks in the Ag case, respectively. Therefore, for the same FER number, $\Delta Z$ on HOPG is nearly the same as that on Ag(111), indicating that the TIAD level on HOPG was not increased while the bias voltage increased, i.e. the electrostatic force could be constant when observing FER. Thus, FER peaks were measured on a stable dome-shaped surface.

Figure 8(a) is a topography image of HOPG taken at 3 V, 1 nA and 5 K, in which the surface consists of a high terrace (bright area) and a low terrace (dark area) due to a step. Figure 8(b) shows a line profile along a 200 Å-long line crossing a step in figure 8(a), revealing that the step height is close to one atomic layer. We took an FER spectrum along the line every 2 Å from left to right under 0.1, 0.5, and 1 nA (see supplementary material), and measured $F_{FER}$ and FER 1 $\Delta E$ in each spectrum. Figure 8(c) presents $F_{FER}$ versus position on the line at three currents. Although the STM feedback was on, $F_{FER}$ still had a slight increase when the tip crossed the step, which is approximately 1.4% of $F_{FER}$ on the low terrace for all three cases in figure 8(c). According to this $F_{FER}$ increase, the position of the step edge can be determined from the maximum of $F_{FER}$, which is nearly identical for three cases in figure 8(c), marked by a dashed line at the position of 154 Å. Figure 8(d) displays FER 1 $\Delta E$ versus position at three currents. With the values in figures 8(c) and (d), we depicted the plots of $D_{HOPG}$ versus position, as displayed in figure 8(e). For comparison, the line profile in figure 8(b) is also shown in figures 8(c), (d), and (e).

At 0.1 nA, the plot shows that $D_{HOPG}$ is nearly constant. The plot at 0.5 nA reveals that $D_{HOPG}$ is nearly constant at most of positions, but presents a triangle shaped variation for some positions; it increases from the position of 104 Å and reaches maximum at 124 Å then decreases. Because the step edge is at 154 Å (dashed line), the increase of $D_{HOPG}$ occurs at the low terrace. Moreover, except the triangle shaped variation, there is no difference for $D_{HOPG}$ at the low and high terraces. Therefore, the step can elevate the height of TIAD on the low terrace as the tip is close to a step, However, $F_{FER}$ should exceed 0.26 V Å to detect this step-induced height elevation, according to figure 8(c). The triangle shaped variation reflects that the van der Waals force is weaker in the vicinity of a step due to less symmetry. The plot at 1 nA demonstrates that the triangle shaped variation becomes more pronounced and the positions at which $D_{HOPG}$ is nearly constant shrink to a range between 0 to

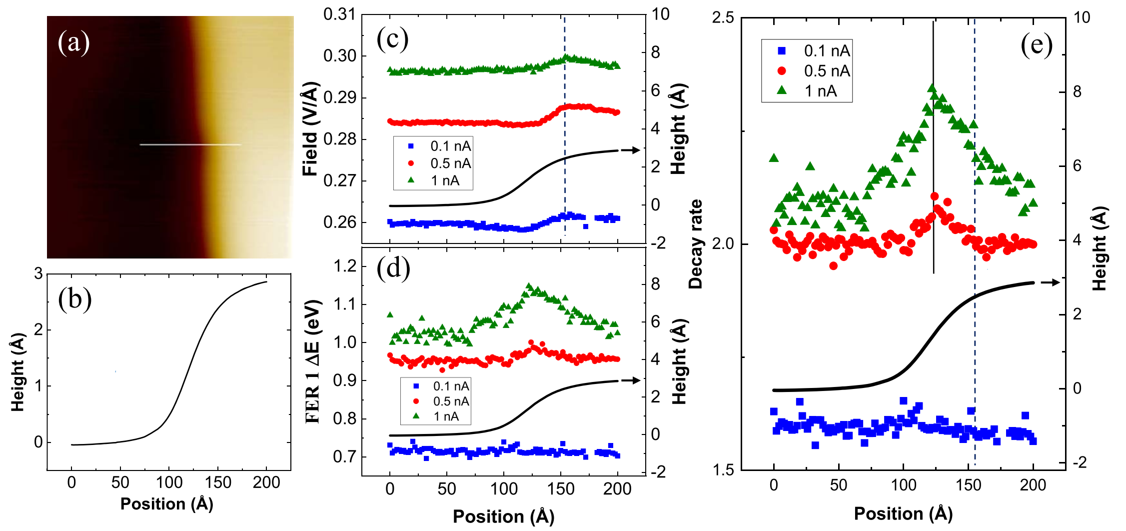


**Figure 8.** (a) Topography image of HOPG taken at 3 V and 1 nA. (b) Line profile along a 200 Å long line crossing a step in (a). (c) $F_{FER}$ versus position on the line at 0.1, 0.5, and 1 nA. (d) FER 1 $\Delta$E versus position at 0.1, 0.5, and 1 nA. (e) The plots of D versus position at 0.1, 0.5, and 1 nA. For comparison, the line profile in (b) is also shown in (c), (d), and (e).

74 Å, displaying that a stronger electrostatic force can extend the area of step-induced height elevation. Moreover, the average $D_{HOPG}$ on the high terrace (154–200 Å) is greater than that on the low terrace (0–74 Å), indicating that due to less symmetry, at the high terrace, the van der Waals force near the step is weaker than that away from the step, but is stronger than that near the step at the low terrace because $F_{FER}$ should be as high as 0.295 V Å to observe this difference, according to figure 8(c). In addition, because the triangle shaped variation results from the step, the lateral position of the highest value in $D_{HOPG}$ is the same as that in the plot at 0.5 nA, as marked by a solid line.

## 4. Conclusions

We demonstrated that FER can be used as a tool to probe the TIAD of an HOPG surface. By measuring FER energies to derive $F_{FER}$ and by extracting FER linewidth, we derived $D_{HOPG}$ to monitor the TIAD of the surface. A higher $D_{HOPG}$ value represents a higher TIAD level. For comparison, we also observed FER on the Ag(111) surface. The derived $D_{Ag}$ was insensitive to the electrostatic force in STM junction, implying that the TIAD on Ag surface is negligible. DFT calculations demonstrated that the DOS of the graphene was considerably higher than that of graphite at the FER 1 energy, signifying that the TIAD rendered the top layer analogous to graphene because the decay rate is proportional to the DOS. It is well known that the electronic structures of two-dimensional (2D) materials are sensitive to the strain [44, 45]. Strain-induced change of the DOS above the vacuum level in 2D materials is expected, implying that FER may be a tool to probe the strain distribution on 2D materials through measuring the decay rate of its wave function.

## Acknowledgments

This work was supported by the Ministry of Science and Technology (Grant No. MOST 109-2112-M-001-049) and Academia Sinica (Grant No. AS-iMATE-109-15), Taiwan, and the ANR and MOST (DEFINE2D project No. ANR-20-CE09-0023, MOST 110-2923-M-002-010). We thank National Center for High-performance Computing of National Applied Research Laboratories in Taiwan for providing computational and storage resources.

## Data availability statement

All data that support the findings of this study are included within the article (and any supplementary files).

## ORCID iDs

Wei-Bin Su https://orcid.org/0000-0002-7555-7634
Chih-Hao Lee https://orcid.org/0000-0002-3898-6421

## References

[1] Limot L, Maroutian T, Johansson P and Berndt R 2003 Surface-state stark shift in a scanning tunneling microscope *Phys. Rev. Lett.* **91** 196801
[2] Ogawa S, Heike S, Takahashi H and Hashizume T 2007 Tip-induced energy shift in Au/Fe(100) quantum wells *Phys. Rev.* B **75** 115319
[3] Su W B, Lu S M, Jiang C L, Shih H T, Chang C S and Tsong T T 2006 Stark shift of transmission resonance in scanning tunneling spectroscopy *Phys. Rev.* B **74** 155330
[4] Chan W Y, Huang H S, Su W B, Lin W H, Jeng H-T, Wu M K and Chang C S 2012 Field-induced expansion deformation in Pb islands on Cu(111): Evidence from energy shift of empty quantum-well states *Phys. Rev. Lett.* **108** 146102
[5] Breitwieser R, Hu Y C, Chao Y C, Li R J, Tzeng Y R, Li L J, Liou S C, Lin K C, Chen C W and Pai W W 2014 Flipping nanoscale ripples of free-standing graphene using a scanning tunneling microscope tip *Carbon* **77** 236
[6] Weng S W, Lin W H, Su W B, Hwu E T, Chen P L, Tsai T R and Chang C S 2014 Estimating young's modulus of graphene with raman scattering enhanced by micrometer tip *Nanotechnology* **25** 255703
[7] Soler J M, Baro A M, García N and Rohrer H 1986 Interatomic forces in scanning tunneling microscopy: giant corrugations of the graphite surface *Phys. Rev. Lett.* **57** 444
[8] Zeng X Z, Peng Y T, Liu L, Lang H J and Cao X A 2018 Dependence of the friction strengthening of graphene on velocity *Nanoscale* **10** 1855
[9] Peng Y T, Zeng X Z, Yu K and Lang H J 2020 Deformation induced atomic-scale frictional characteristics of atomically thin two-dimensional materials *Carbon* **163** 186
[10] Gundlach K H 1966 Zur berechnung des tunnelstroms durch eine trapezformige potentialstufe *Solid-State Electron.* **9** 949
[11] Binnig G, Frank K H, Fuchs H, Garcia N, Reihl B, Rohrer H, Salvan F and Williams A R 1985 Tunneling spectroscopy and inverse photoemission - image and field states *Phys. Rev. Lett.* **55** 991
[12] Becker R S, Golovchenko J A and Swartzentruber B S 1985 Electron interferometry at crystal-surfaces *Phys. Rev. Lett.* **55** 987
[13] Bobrov K, Mayne A J and Dujardin G 2001 Atomic-scale imaging of insulating diamond through resonant electron injection *Nature* **413** 616
[14] Liu S, Wolf M and Kumagai T 2018 Plasmon-assisted resonant electron tunneling in a scanning tunneling microscope junction *Phys. Rev. Lett.* **121** 226802
[15] Barimar P S N, Naydenov B, Li J and Boland J J 2017 Spreading resistance at the nano-scale studied by scanning tunneling and field emission spectroscopy *Appl. Phys. Lett.* **110** 263111
[16] Coombs J, Gimzewski J, Reihl B, Sass J and Schlittler R 1988 Photon emission experiments with the scanning tunneling microscope *J. Microsc.* **152** 325
[17] Martínez-Blanco J and Fölsch S 2015 Light emission from Ag(111) driven by inelastic tunneling in the field emission regime *J. Phys. Condens. Matter* **27** 255008
[18] Leon C C, Rosławska1 A, Grewal A, Gunnarsson O, Kuhnke K and Kern K 2019 Photon superbunching from a generic tunnel junction *Sci. Adv.* **5** eaav4986
[19] Pascual J I, Corriol C, Ceballos G, Aldazabal I, Rust H P, Horn K, Pitarke J M, Echenique P M and Arnau A 2007 Role of the electric field in surface electron dynamics above the vacuum level *Phys. Rev.* B **75** 165326
[20] Wahl P, Schneider M A, Diekhoner L, Vogelgesang R and Kern K 2003 Quantum coherence of image-potential states *Phys. Rev. Lett.* **91** 106802
[21] Schouteden K and Van Haesendonck C 2009 Quantum confinement of hot image potential state electrons *Phys. Rev. Lett.* **103** 266805
[22] Stepanow S, Mugarza A, Ceballos G, Gambardella P, Aldazabal I, Borisov A G and Arnau A 2011 Localization, splitting, and mixing of field emission resonances induced by alkali metal clusters on Cu(100) *Phys. Rev.* B **83** 115101
[23] Craes F, Runte S, Klinkhammer J, Kralj M, Michely T and Busse C 2013 Mapping Image Potential States on Graphene Quantum Dots *Phys. Rev. Lett.* **111** 056804
[24] Lin C L, Lu S M, Su W B, Shih H T, Wu B F, Yao Y D, Chang C S and Tsong T T 2007 Manifestation of work function difference in high order Gundlach oscillation *Phys. Rev. Lett.* **99** 216103
[25] Huang H S, Chan W Y, Su W B, Hoffmann G and Chang C S 2013 Measurement of work function difference between Pb/Si(111) and Pb/Ge/Si(111) by high-order Gundlach oscillation *J. Appl. Phys.* **114** 214308
[26] Schulz F, Drost R, Hämäläinen S K, Demonchaux T, Seitsonen A P and Liljeroth P 2014 Epitaxial hexagonal boron nitride on Ir(111): A work function template *Phys. Rev.* B **89** 235429
[27] Neilson J *et al* 2019 Nitrogen-doped graphene on copper: edge-guided doping process and doping-induced variation of local work function *J. Phys. Chem.* C **123** 8802
[28] Schouteden K, Amin-Ahmadi B, Li Z, Muzychenko D, Schryvers D and Van Haesendonck C 2016 Electronically decoupled stacking fault tetrahedra embedded in Au(111) films *Nat. Commun.* **7** 14001
[29] Gutiérrez C, Brown L, Kim C J, Park J and Pasupathy A N 2016 Klein tunneling and electron trapping in nanometre-scale graphene quantum dots *Nat. Phys.* **12** 3806
[30] Zhang Q, Yu J, Ebert P, Zhang C, Pan C R, Chou M Y, Shih C K, Zeng C and Yuan S 2018 Tuning Band gap and work function modulations in monolayer hBN/Cu(111) heterostructures with moire patterns *ACS Nano* **12** 9355
[31] Borca B, Castenmiller C, Tsvetanova M, Sotthewes K, Rudenko A N and Zandvliet H J W 2020 Image potential states of germanene *2D Mater.* **7** 035021
[32] Sagisaka K and Fujita D 2008 Unusual mosaic image of the Si(111)-(7 × 7) surface coinciding with field emission resonance in scanning tunneling microscopy *Phys. Rev.* B **77** 205301
[33] Rienks E D L, Nilius N, Rust H P and Freund H J 2005 Surface potential of a polar oxide film: FeO on Pt(111) *Phys. Rev.* B **71** 241404
[34] Su W B, Lu S M, Lin C L, Shih H T, Jiang C L, Chang C S and Tsong T T 2007 Interplay between transmission background and Gundlach oscillation in scanning tunneling spectroscopy *Phys. Rev.* B **75** 195406

[35] Chan W Y, Lu S M, Su W B, Liao cc, Hoffmann G, Tsai T R and Chang C S 2017 Sharpness-induced energy shifts of quantum well states in Pb islands on Cu(111) *Nanotechnol.* **28** 095706

[36] Lu S M, Chan W Y, Su W B, Pai W W, Liu H L and Chang C S 2018 Characterization of external potential for field emission resonances and its applications on nanometer-scale measurements *New J. Phys.* **20** 043014

[37] Su W B, Lin C L, Chan W Y, Lu S M and Chang C S 2016 Field enhancement factors and self-focus functions manifesting in field emission resonances in scanning tunneling microscopy *Nanotechnol.* **27** 175705

[38] Su W B, Lu S M, Jeng H T, Chan W Y, Chang H H, Pai W W, Liu H L and Chang C S 2020 Observing quantum trapping on $MoS_2$ through the lifetimes of resonant electrons: revealing the Pauli exclusion principle *Nanoscale Adv.* **2** 5848

[39] Dougherty D, Maksymovych P, Lee J, Feng M, Petek H and Yates J Jr 2007 Tunneling spectroscopy of Stark-shifted image potential states on Cu and Au surfaces *Phys. Rev. B* **76** 125428

[40] Ooi N, Rairkar A and Adams J B 2006 Density functional study of graphite bulk and surface properties *Carbon* **44** 231

[41] Rut'kov E V, Afanas'eva E Y and Gall N R 2020 Graphene and graphite work function depending on layer number on Re *Diam. Relat. Mater.* **101** 107576

[42] Sakurai J J 1985 *Modern Quantum Mechanics* 1st ed (New York: Benjamin- Cummings) 104

[43] Belaidi S, Girard P and Leveque G 1997 Electrostatic forces acting on the tip in atomic force microscopy: Modelization and comparison with analytic expressions *J. Appl. Phys.* **81** 1023

[44] Yang S, Chen Y and Jiang C 2021 Strain engineering of two-dimensional materials: Methods, properties, and applications *InfoMat* **3** 397

[45] Zhang C, Li M Y, Tersoff J, Han Y, Su Y, Li L J, Muller D A and Shih C K 2018 Strain distributions and their influence on electronic structures of WSe2–MoS2 laterally strained heterojunctions *Nat. Nanotechnol.* **13** 152